From Rare Events to a Population: Discovering Overlooked Extragalactic Magnetar Giant Flare Candidates in Archival Fermi Gamma-ray Burst Monitor Data

Aaron C. Trigg¹, Eric Burns², Michela Negro², Suman Bala³, P.N. Bhat⁴, William H. Cleveland³, Dmitry D. Frederiks⁵, Adam Goldstein³, Boyan A. Hristov⁴, Daniel Kocevski⁶, Niccolò Di Lalla⁷, Stephen Lesage^{4,8}, Bagrat Mailyan⁹, Eliza Neights^{10,11}, Nicola Omodei⁷, Oliver J. Roberts³, Lorenzo Scotton⁴, Dmitry S. Svinkin⁵, and Joshua Wood⁶

- NASA Postdoctoral Program Fellow, NASA Marshall Space Flight Center, Huntsville, AL, 35812, USA e-mail: aaron.c.trigg@nasa.gov
- ² Department of Physics & Astronomy, Louisiana State University, Baton Rouge, LA 70803, USA
- ³ Science and Technology Institute, Universities Space Research Association, Huntsville, AL 35805, USA
- Center for Space Plasma and Aeronomic Research, University of Alabama in Huntsville, Huntsville, AL 35899, USA
- ⁵ Ioffe Institute, 26 Politekhnicheskaya, St. Petersburg, 194021, Russia
- ⁶ ST12 Astrophysics Branch, NASA Marshall Space Flight Center, Huntsville, AL 35812, USA
- W. W. Hansen Experimental Physics Laboratory, Kavli Institute for Particle Astrophysics and Cosmology, Department of Physics and SLAC National Accelerator Laboratory, Stanford University, Stanford, CA 94305, USA
- ⁸ Department of Space Science, University of Alabama in Huntsville, 320 Sparkman Drive, Huntsville, AL 35899, USA
- Department of Aerospace, Physics and Space Sciences, Florida Institute of Technology, Melbourne, FL 32901, USA
- Department of Physics, The George Washington University, 725 21st St NW, Washington, DC 20052, USA
- Astrophysics Science Division, NASA Goddard Space Flight Center, 8800 Greenbelt Road, Greenbelt, MD 20771, USA

ABSTRACT

Magnetar giant flares are rare, extremely bright bursts of gamma-rays from highly magnetized neutron stars. These events are challenging to identify because, at extragalactic distances, they can appear similar to other astrophysical phenomena. Only a handful have been confidently identified to date, limiting our understanding of their origin and physical properties. This study focuses on expanding the sample of known events and enabling a more detailed characterization of their observational features and intrinsic properties, while introducing significant improvements in the methods used to identify and analyze them. When applied to archival data from the Gamma-ray Burst Monitor (GBM) on the *Fermi* Gamma-ray Space Telescope, this approach added four previously unidentified events the known sample, expanding the total to 13 MGFs. This demonstrates both the effectiveness of the method and the likelihood that additional magnetar giant flares remain hidden in existing gamma-ray burst catalogs. We utilize this expanded sample to gain a deeper understanding of the broader population of magnetar giant flares. We develop a statistical modeling framework that combines previously considered data with modern observations from *Fermi*/GBM. The model accounts for instrumental sensitivity and the expected diversity in event characteristics. We infer a volumetric rate of events above 1.2×10^{44} erg of $R_{MGF} = 5.5^{+4.5}_{-2.7} \times 10^{5}$ Gpc $^{-3}$ yr $^{-1}$. The results show that individual magnetars must produce multiple flares throughout their lifetimes, reinforcing the idea that these are recurring phenomena rather than singular explosive events. Expanding the sample of known magnetar giant flares improves our understanding of magnetars and their role in other astrophysical phenomena, including possible links to fast radio bursts, gravitational waves, and the creation of heavy elements in extreme astrophysical environments.

Key words. gamma-ray bursts – magnetars – neutron stars

1. Introduction

A core collapse supernova (CCSN) marks the catastrophic end of a massive star, resulting in the formation of either a black hole or a neutron star (NS). In some cases these NSs are characterized by the strongest persistent magnetic fields in the cosmos, exceeding 10¹⁴ G (Usov 1984; Duncan & Thompson 1992; Paczynski 1992; Thompson & Duncan 1995, 1996; Kaspi & Beloborodov 2017). These NSs are classified as magnetars. The densities and field strengths of these compact remnants enable studies of physics inaccessible in laboratory environments. More than two dozen magnetars have been identified in star-forming regions of the Milky Way (Gaensler 2004) and Large Magellanic Cloud (LMC; Olausen & Kaspi 2014), where they produce a variety of high-energy transient emissions. The diverse range of

phenomena includes sub-second bursts, burst "storms" made up of hundreds to thousands of bursts over several minutes, and the most extreme example of magnetar emission, the magnetar giant flare (MGF; Kaspi & Beloborodov 2017; Negro et al. 2024).

Magnetar giant flares initially display a brief, millisecondlong gamma-ray peak that is spectrally harder than the typical magnetar emission, with isotropic-equivalent energies $E_{\rm iso} \sim 10^{44} - 10^{46}$ erg. The initial hard, high-energy peak then transitions to a weaker, softer tail that last several minutes. This tail displays a periodic signal due to modulation by the spin period of the source NS (Hurley et al. 1999; Palmer et al. 2005). Since the first observation of a MGF, localized to the magnetar SGR 0526–66 in the LMC on 3 March 1979 (Mazets et al. 1979), two additional MGFs have been associated with the magnetars SGR 1900+14 (Hurley et al. 1999; Feroci et al. 1999) and SGR 1806-20 (Palmer et al. 2005; Frederiks et al. 2007a) in the Milky Way. The initial peaks for all three events exhibited extremely high flux rates that saturated the detectors on nearly all observing instruments.

However, at extragalactic distances, the rotationally modulated tail of an MGF is too faint to be detected by current instruments without rapid identification and re-pointing (Negro et al. 2024; Trigg et al. 2025), and has yet to be observed. Therefore, a distant event lacking such a tail would appear similar to, and potentially misidentified as, a cosmological short gammaray burst (sGRB; Mazets et al. 1982; Duncan 2001; Hurley et al. 2005; Palmer et al. 2005; Hurley 2011), a phenomenological class defined by transient flashes of high-energy photons in the 10 keV-10 MeV range that last less than ~2 seconds believed to originate from mergers of compact object binaries such as NS-NS or NS-black hole (BH) systems (Kouveliotou et al. 2012; Kouveliotou et al. 1993; Eichler et al. 1989; Fong et al. 2015; Abbott et al. 2017a,b; Goldstein et al. 2017). This limitation requires alternative methods for identifying MGFs that originate outside of the Milky Way: localizing sGRBs to nearby star-forming galaxies.

Six extragalactic bursts have been classified as MGFs, relying primarily on their spatial coincidence with star-forming galaxies, and supported by their temporal and spectral properties. Five were localized by the Interplanetary Network of gamma-ray satellites (IPN; Hurley et al. 2013) and one by the International Gamma-ray Astrophysics Laboratory (INTEGRAL), enabling associations with nearby star-forming galaxies. These candidates are GRB 051103, associated with M81 (Ofek et al. 2006; Frederiks et al. 2007b; Hurley et al. 2010), GRB 070201, associated with the galaxy M31 (Mazets et al. 2008; Ofek et al. 2008), GRB 070222, associated with M83 (Burns et al. 2021), GRB 200415A and GRB 180128A, both localized to NGC 253 (Svinkin et al. 2021; Roberts et al. 2021; Trigg et al. 2024), and GRB 231115A, associated with M82 (Mereghetti et al. 2024; Trigg et al. 2025).

A pressing question is how frequently these events occur throughout the cosmos. This frequency can be expressed as a volumetric rate, the number of flares per unit volume per year. Estimating this rate is critical for understanding the population of MGFs, particularly given the small number of observed events. The first quantitative measurement of the volumetric rate of MGFs was presented by Burns et al. (2021), who found a rate of $R_{\rm MGF} = 3.8^{+4.0}_{-3.1} \times 10^5~\rm Gpc^{-3}~\rm yr^{-1}$ above a minimum isotropic-equivalent energy of $E_{\rm iso,min} = 3.7 \times 10^{44} \rm erg$. Understanding the rate of MGFs offer direct insights into magnetar energy release mechanisms, as their temporal structure and energetics reflect processes such as magnetic reconnection and crustal failure induced by internal magnetic stresses (Thompson & Duncan 1995, 1996). These signatures constrain models of how energy is transferred from the stellar interior to the magnetosphere and radiated away.

The study of MGFs is also tightly linked to other astrophysical phenomena. Theoretical models predict that MGFs may emit gravitational wave (GW) signals, either as bursts during the flare onset or via excitation of NS normal modes (Abbott et al. 2007, 2019; Macquet et al. 2021; Beniamini et al. 2025). These modes correspond to large-scale oscillations of the NS, including crustal shear vibrations and global seismic activity, which can be triggered by the sudden reconfiguration of the magnetic field or fracturing of the solid crust during an MGF. Such events involve rapid, asymmetric motions of dense matter, producing the time-varying quadrupole moment necessary for GW emission. Next-generation GW observatories (Punturo et al. 2010)

may detect such signals, offering unique insight into the NS interior and crust, with implications for constraining the equation of state of dense matter (Patra et al. 2020).

MGFs have also been shown to be responsible for the formation of heavy elements like gold, platinum, and uranium via the rapid neutron capture process (r-process; Cameron 1957; Burbidge et al. 1957). The MGF from SGR 1806-20 has been shown to produce conditions suitable for r-process nucleosynthesis: baryon-loaded ejecta expelled during a flare can undergo rapid neutron capture as it decompresses, particularly in the fast outer layers where a hot, α -rich freeze-out enables the formation of both light and heavy nuclei (Cehula et al. 2024; Patel et al. 2025). Although unlikely to dominate Galactic heavy element production, such flares could contribute to early chemical enrichment given their short delay times after star formation. The early production of heavy elements may have played a critical role in sustaining molten planetary cores through radiogenic heating (Stevenson 2008), which are essential for the generation of magnetic fields. Such fields, in turn, help shield planetary atmospheres and create conditions favorable for the emergence of

Magnetars are also associated with some fast radio bursts (FRBs), as demonstrated by FRB 200428 from SGR 1935+2154—a Galactic magnetar that emitted a coincident radio burst and X-ray outburst (Popov et al. 2018; Bochenek et al. 2020). However, this event was not an MGF, but rather a lower-energy outburst from a magnetar. No confirmed MGFs, Galactic or extragalactic, have yet shown associated FRB emission, even when simultaneous radio observations were available (Curtin & Chime/FRB Collaboration 2023). Establishing whether MGFs can, or routinely do, produce FRBs remains a key question in understanding the origin of these millisecond-duration radio flashes.

By building and characterizing a larger population of MGFs, we can place tighter constraints on their rates, energetics, and possible magnetar progenitors. Expanding the sample of MGFs reduces Poisson uncertainty in measuring their intrinsic rates and improves constraints on their energetics distribution. These improvements enhance the precision of forward-folding models, provide data to help resolve parameter correlations, and yield more robust insight into the physical processes underlying MGF production and magnetar evolution. By doing so, we can gain a better understanding of how magnetars form, how often they flare, and under what conditions they might produce related transients, such as FRBs. A more complete MGF sample will support the design of future GRB instruments and inform multimessenger searches by contextualizing potential gravitational-wave or neutrino signals.

We conduct a systematic archival search of the Fermi Gamma-ray Burst Monitor (GBM; Meegan et al. 2009) sGRB dataset, guided by an empirical evaluation of the known extragalactic MGF population (Section 2). This search was motivated by the prior identification of GRB 180128A in an initial exploratory search (Trigg et al. 2024), demonstrating that GBM could reveal additional low-fluence events not previously identified as MGFs. Then, building on the forward-folding population analysis of Burns et al. (2021), we integrate these newly identified GBM candidates with previously published IPN events to construct a more complete sample. This combined dataset enables improved statistical constraints on the volumetric rate, minimum energetics, and energy distribution of MGFs while accounting for instrument-specific detection probabilities and spectral variation. By unifying GBM and IPN detections within a self-consistent Markov Chain Monte Carlo (MCMC) framework, our approach provides the most robust characterization of the extragalactic MGF population to date (Section 3). Section 4 discusses the implications of our results for magnetar formation, energetics, and recurrence, while Section 5 summarizes the key conclusions and outlines future directions for the study of extragalactic MGFs.

2. Archival Data Search for Extragalactic Magnetar Giant Flares

In our refined search for extragalactic MGFs in archival data, we maintain our focus on the <code>Fermi/GBM</code>. <code>Fermi/GBM</code> is comprised of 12 uncollimated thallium-doped sodium iodide (NaI) detectors and two bismuth germanate (BGO) detectors, mounted on opposite sides of the spacecraft to ensure coverage of the full, unocculted sky at higher energies. Each NaI detector is sensitive to photons in the \sim 8–900 keV range, while the BGO detectors cover a higher-energy range of approximately 0.25–40 MeV. Together, the NaI and BGO enable the detection and spectral characterization of a wide variety of gamma-ray transients.

GBM continuously monitors the count rates in each detector and triggers when a statistically significant rate increase is observed in at least two NaI detectors. The on-board trigger threshold corresponds to a flux of roughly a few photons cm $^{-2}$ s $^{-1}$ in the 50–300 keV band (for a 1 s peak interval). The sensitivity of Fermi/GBM in the 50–300 keV band is sufficient to detect the vast majority of GRBs, including weaker short events. We focus on the Time-Tagged Event (TTE) data, which records the time and energy of each photon detection during a burst with microsecond timing precision. Each TTE event includes an energy channel (out of 128 channels) and an absolute time stamp with 2 μ s resolution.

The fine temporal and spectral resolution of *Fermi*/GBM, combined with its broad sky coverage and high sensitivity to sGRBs, offers a unique opportunity to search for extragalactic MGFs hidden among the broader population of sGRBs. GBM is the most prolific detector of short GRBs, providing an unparalleled dataset for studying these events. Although *Fermi*/GBM is not instantaneously all-sky, typically covering about two-thirds of the sky at any given moment, it continuously monitors a large fraction of the sky with high sensitivity. This enables the detection of bright short-duration events across a significant cosmological volume, making GBM an ideal instrument for archival MGF searches.

However, given that MGFs account for only $\sim 2\%$ of the total sGRB sample (Burns et al. 2021), directly attempting to associate every detected sGRB with nearby galaxies would be inefficient and would result in enormous losses of statistical power. To address this, we apply a down-selection procedure that filters for bursts with characteristics expected of extragalactic MGFs before attempting precise localization. This targeted approach reduces the population of interest by up to an order of magnitude, improving the sensitivity and efficiency of follow-up searches for host galaxy associations while mitigating false positives.

Guided by characteristic observational signatures, we systematically scour the archival *Fermi*/GBM dataset for previously unidentified MGFs. Here, we describe the data and methods used to discern MGF candidates from the broader population of GBM triggers.

2.1. Refined Search

With GRB 180128A and GRB 231115A now added to the sample of known extragalactic MGFs, we turn to refining selection criteria to search for similar events within the *Fermi/GBM* catalog more robustly. This refinement required accounting for both the observed properties of the MGF population and the temporal and spectral limitations of the observing instruments. We utilize a Bayesian Blocks-based approach (BB; Scargle et al. 2013) as a temporal analysis selection filter, focusing on rise time and duration. For our revised search, we analyze all GBM triggers that occurred prior to March 2025 using TTE data available in the *Fermi/GBM* catalog. To clarify the event selection process, Figure 1 presents a flowchart detailing the selection criteria and the number of bursts that pass each step.

To calibrate our selection criteria for extragalactic MGFs, we require a representative sample of confirmed events. Given that Fermi/GBM has only observed three extragalactic MGFs (GRB 200415A, GRB 180128A, and GRB 231115A) we must look to another instrument that has high-quality observations of the remaining three bursts. The best such instrument is Konus/Wind (Aptekar et al. 1995), which has detected and characterized multiple confirmed extragalactic MGFs. Since its launch in 1994, Konus/Wind has provided all-sky gamma-ray coverage using two NaI detectors oriented toward the ecliptic poles. In triggered mode, the instrument records highresolution light curves in three energy bands, G1 (18-70 keV), G2 (70-300 keV), and G3 (300-1100 keV), over a ~230 s window spanning from T_0 – 0.512 s to T_0 + 229.632 s. The time resolution steps from 2 ms to 256 ms over the course of the burst, and 64 multichannel spectra are acquired from 10 keV to 10 MeV with adaptive integration times (Aptekar et al. 1995; Svinkin et al. 2021).

We define the Konus sample as the four confirmed extragalactic MGFs observed by Konus/Wind for which we have data: GRB 051103, GRB 070201, GRB 070222, and GRB 200415A (Svinkin et al. 2016; Svinkin et al. 2021). For GRB 200415A, which GBM also observed, we utilize the Konus/Wind data to maintain consistency across the sample. The inclusion of high-quality Konus/Wind data allows us to refine our selection filters based on well-characterized MGF properties. To quantify the temporal structure of each event, we applied a BB algorithm to the Konus/Wind light curves. This produced consistent, instrument-independent characterizations of each burst's timing behavior.

Given that $N_{\rm photons} \propto 1/d^2$ when fixing intrinsic brightness, we expect the number of detected counts for a given sGRB to decrease with distance. As the counts diminish, the BB analysis becomes more likely to identify fewer significant bins, often resulting in longer-duration bins where signal significance is reduced. To empirically determine appropriate temporal cuts, we took the full sample of known extragalactic MGFs (from both the GBM and Konus datasets). We attenuated their photon fluxes from the distances to their respective host galaxies to a distance of 50 Mpc, in 0.5 Mpc increments. Our burst attenuation analysis allowed us to evaluate the distance at which our BB-based detection algorithm would fail to identify the known MGFs. We defined failure as the presence of fewer than three BB bins (i.e., when no statistically significant temporal structure remains detectable). However, our analysis also shows that as distances increase by an order of magnitude, the BB binning for MGFs can appear as bright, isolated spikes, with the most significant bin typically spanning 10–30 ms.

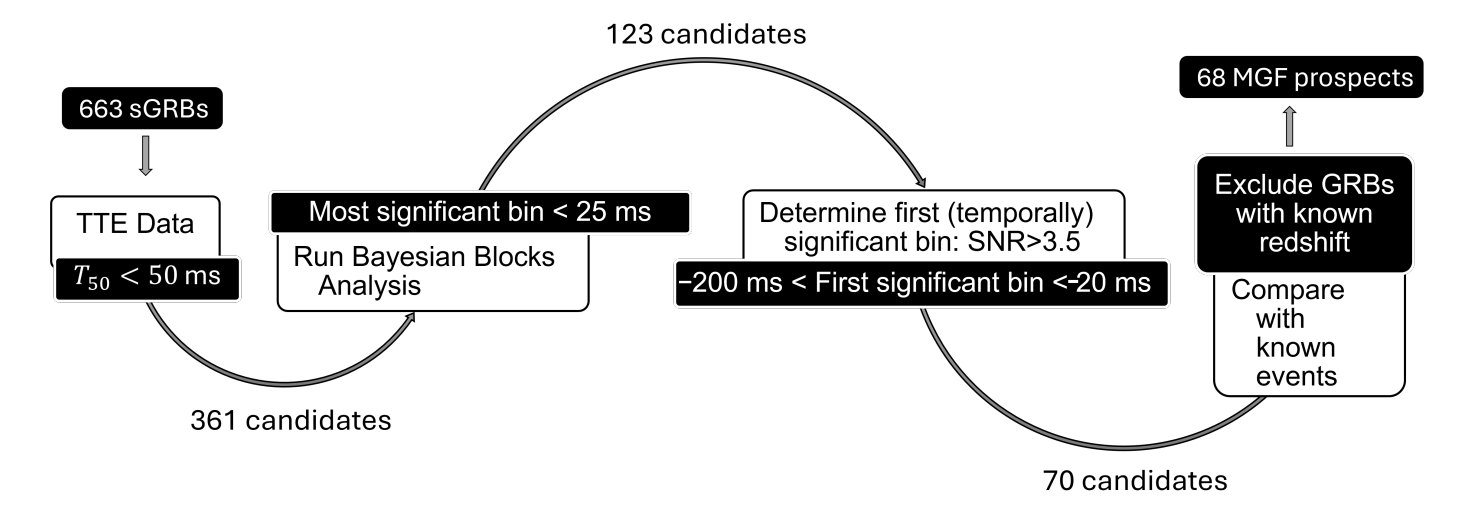


Fig. 1. Flowchart illustrating the refined selection criteria used to identify MGF candidates from the *Fermi*/GBM sGRB sample. Starting from 663 sGRBs with available TTE data, a series of temporal cuts is applied using BB analysis. GRBs with known redshift are excluded, yielding 68 MGF prospects.

Beginning our search of GBM archival data, we use the bcat detector mask¹, which reports the good detectors for each burst as determined by the GBM team. Good detectors are defined as NaI detectors with a boresight angle within 60 degrees of the source. The bcat files provide basic burst information such as duration, peak flux, and fluence, and include only data from these good-viewing detectors. We then select the appropriate BGO detector based on which side of *Fermi* has the greater number of selected NaI detectors. We adopt a uniform bin size of 2 ms for all light curves. This resolution preserves the prompt peak while allowing us to probe finer temporal structure within the burst.

The first parameter we examined was the T_{50} duration. The T_{50} is the duration over which 50% of the burst fluence accumulates, starting when 25% of the total fluence is detected, measured between 50 keV and 300 keV. However, when applying this cut to the full GBM trigger catalog of sGRBs, we found that significantly fewer bursts from earlier in the mission satisfied this criterion. This discrepancy arises from evolving choices in how finely burst durations were evaluated-particularly the temporal resolution of the light curves used to compute $T_{50,GBM}$. In the early catalog, the fixed time binning sometimes exceeded the actual burst duration, which limited the precision of duration measurements for the shortest bursts. To ensure consistent and accurate treatment of T_{50} durations across the entire dataset, we recalculated the durations $(T_{50,BB})$ for the full sGRB sample using a BB-based approach, similar to the battblocks² algorithm used to estimate burst durations for the Swift Burst Alert Telescope (Barthelmy et al. 2005).

We start by selecting events in the full catalog with $T_{50,GBM} \le 250$ ms. This duration was chosen due to no known MGF having a full duration beyond ~150 ms, allowing us to reduce the initial sample considered from 663 sGRBs to 361 bursts. To improve accuracy, we apply partial-bin interpolation when determining $T_{50,BB}$ durations. This method assumes a constant count rate within each BB bin. If the cumulative counts cross the 25%

or 75% thresholds that define the T_{50} within a bin, we solve for the precise time at which that threshold is reached, rather than assigning all counts to the bin edge. At the millisecond timescales relevant to our analysis, this approach yields a more robust estimate of T_{50} than simple linear interpolation. Examining the distribution of $T_{50,BB}$ durations among known MGFs, we observe that none exceed ~ 40 ms. Thus, we conservatively impose a selection criterion of $T_{50,BB} \le 50$ ms.

The next parameter we set out to refine was the duration of the bright, main spike of the burst. This corresponds to the BB bin with the highest count rate per unit time, referred to as the most significant BB bin. To account for the results of our attenuation analysis, we first include in our sample any burst that displays a single significant BB bin, as such cases may represent distant MGFs for which reduced photon statistics obscure finer structure. For all other bursts, we track the peak duration (as measured by the most significant BB bin) as a function of distance. The attenuation analysis also revealed that, out to 9.5 Mpc, all events in the sample maintained a peak duration of ≤ 25 ms. Beyond this distance, only GRB 231115A exceeded this threshold, with a peak duration of 42 ms at 20 Mpc; a distance within the detectable range for Fermi/GBM, but beyond the range where events can typically be confidently identified due to localization limitations. Based on these results, we adopted a peak duration cut of 25 ms for multi-BB-bin bursts. These considerations result in a sample of 123 prospective candidates.

To ensure we only select events with sharp rise times similar to those seen in the extragalactic MGF population the final parameter under consideration is the first significant bin (FSB). The initial criterion–removing bursts with a bin of signal-to-noise ratio ≥3.5 occurring more than 10 ms before the main peak–was intended to select events with fast rise times, consistent with empirical observations of known MGFs, where the most significant pulse typically occurs first. We therefore retained the FSB-based cut to exclude bursts with early-rising components inconsistent with the observational and theoretical profile.

We therefore implement a selection criterion that excludes any burst containing a significant bin between 200 ms and 20 ms prior to the main peak. This approach allows us to preserve potential MGFs exhibiting precursor emission while ensuring that

https://heasarc.gsfc.nasa.gov/w3browse/fermi/ fermigbrst.html

https://heasarc.gsfc.nasa.gov/docs/software/ lheasoft/help/battblocks.html

only bursts with sharp rise-times are selected. Applying this criterion to our down-selected sample, we are left with 70 remaining prospective MGF candidates. We then manually excluded two bursts: GRB 150101B, which is a likely NS-NS merger (Burns et al. 2018), and GRB 150101A, which exhibited an X-ray afterglow and is associated with a host galaxy at z=0.426, confirming its cosmological origin. This refinement resulted in a final sample of 68 MGF candidates.

2.2. Galaxy association

To assess the likelihood that each of the 68 MGF candidates originated from a nearby star-forming galaxy, we implemented the False Alarm Rate (FAR) significance test described in Burns et al. (2021) (see also Negro & Burns 2023; Trigg et al. 2024). For each GRB, we computed a ranking statistic, Ω , defined as the probability-weighted overlap between the GRB localization probability distribution P_i^{GRB} and the expected distribution of extragalactic MGFs, P_i^{MGF} . That is, $P_i^{\text{MGF}} \propto \text{SFR} \times \text{PDF}(E_{\text{iso}}(D,S))$ where D is the host galaxy distance and S the fluence. Each local galaxy, taken from Leroy et al. (2019), is weighted linearly by its star-formation rate (SFR), equally distributed over its apparent size, and by the prevalence of MGFs, which is inferred from the E_{iso} from the given galaxy distance and GRB fluence pairing. All galaxies in the sample are placed on the sky to create P_i^{MGF} . The resulting Ω values were then compared to a background distribution created from 45,000 randomized galaxy distributions, preserving local structure and global SFR distributions.

As shown in Figure 2, which shows the distribution of candidate Ω values (black curve), we define candidate significance based on their location relative to the 99.73% background exclusion contour, corresponding to a 3σ (light blue) and 1σ (dark blue) contour separation line. These confidence intervals are derived from the randomized background trials, following the methodology for generating random realizations that preserve spatial statistical properties as outlined in Burns et al. (2021). Using the cleanest separation region in Ω space, we identify a cut near the boundary, providing a statistically motivated threshold for classifying events as strong MGF candidates. After assigning host galaxies to the full candidate sample using the method described above, we repeat the host association procedure for each of the bursts above the 3σ threshold individually. This step ensures that associations for the most significant events are robust and not biased by bulk-sample assumptions.

A summary of the top-ranked bursts, their host association significance percentages, Ω values, and associated spectral parameters is provided in Table 1. The spectral fits were performed using a time-integrated Comptonized (COMPT; Gruber et al. 2014) model, or drawn from published values where available. The COMPT function exhibits a power-law behavior characterized by an index α , with an exponential cutoff at a characteristic energy $E_{\rm p}$ of the spectral peak of a νF_{ν} representation.

GRB 231115A, GRB 200415A, and GRB 180128A, three known extragalactic MGFs, are robustly recovered in this analysis, each with Ω values well above the 3σ false alarm threshold. Their temporal and spectral properties remain consistent with expectations for MGF emission and provide an important benchmark for candidate evaluation.

An additional four bursts exhibit Ω values that fall just outside the 3σ confidence region of the population distribution, indicating that while their galaxy associations are less significant than the strongest candidates, these track star-forming regions more than expected by chance. Each of these bursts is well fit by

a COMPT spectral model (Table 2), consistent with the behavior of confirmed extragalactic MGFs. The values for the spectral models, three of which are taken from existing catalogs and one obtained from a spectral analysis performed in this work (GRB 200423A), all exhibit $E_{\rm p}$ and α values within the range observed for the known population, further supporting their classification as plausible MGF candidates.

Taken together, these results reinforce the growing body of evidence that a small but significant fraction of sGRBs detected by *Fermi*/GBM originate from extragalactic MGFs. Given that our sample consists of numerous bursts with extremely poor localizations, which preclude them from consideration as MGF candidates, we estimate a lower limit of 1.1%. This result is consistent with the previously reported 2% estimate by Burns et al. (2021). The strongest candidates exhibit both high Ω values and spectral characteristics consistent with MGF emission.

Our initial expectation was that an archival search would primarily recover fainter MGF candidates—those missed during real-time analysis due to marginal fluence or poor localization. This was broadly borne out: many of the newly identified events exhibit lower fluence and simplified temporal structure, consistent with distant or sub-threshold flares. However, a subset of the bursts are sufficiently bright that they may warrant follow-up searches for additional detections for possible localization improvement.

While none of the four newly identified events can be unambiguously classified as MGFs, they are consistent with expectations for extragalactic flares and significant on a population level, expanding the available sample for population inference. These findings provide a statistically robust foundation for constraining the volumetric rate, energetics, and PL distribution of the extragalactic MGF population, as explored in Section 3. The complete set of MGFs used in this analysis is outlined in Table 2, which forms the basis for all subsequent modeling.

3. Population Analysis

Constraining the volumetric rate and minimum isotropicequivalent total energy release for extragalactic MGFs requires a forward-folding modeling framework that accounts for instrumental sensitivity, spectral diversity, and selection effects. Observed samples of MGF candidates are sparse and heterogeneous, drawn from instruments with differing sky coverage, sensitivities, and triggering algorithms. These limitations make population-level inference challenging, particularly when attempting to estimate intrinsic properties from detections subject to severe and energy-dependent selection biases. Moreover, while the intrinsic energetics distribution of MGFs is most naturally expressed in terms of isotropic-equivalent total energy, detector thresholds and recovery efficiencies are fundamentally tied to photon space, as these are photon-counting instruments. The significant spectral variation observed across different MGFs must be taken into consideration when translating between intrinsic properties and observables.

The initial effort by Burns et al. (2021) introduced such a forward-folding modeling approach. That study simulated synthetic MGF populations originating from galaxies within 5 Mpc, using a galaxy catalog to draw source locations, with $E_{\rm iso}$ drawn from a PL distribution and event rates scaled to each galaxy's SFR. Detectability was evaluated using a fixed energy fluence threshold representative of generalized IPN sensitivity, and sample completeness was assessed accordingly. While this approach marked a critical step forward, it avoided consideration of spectral variation entirely by remaining in energy fluence space and

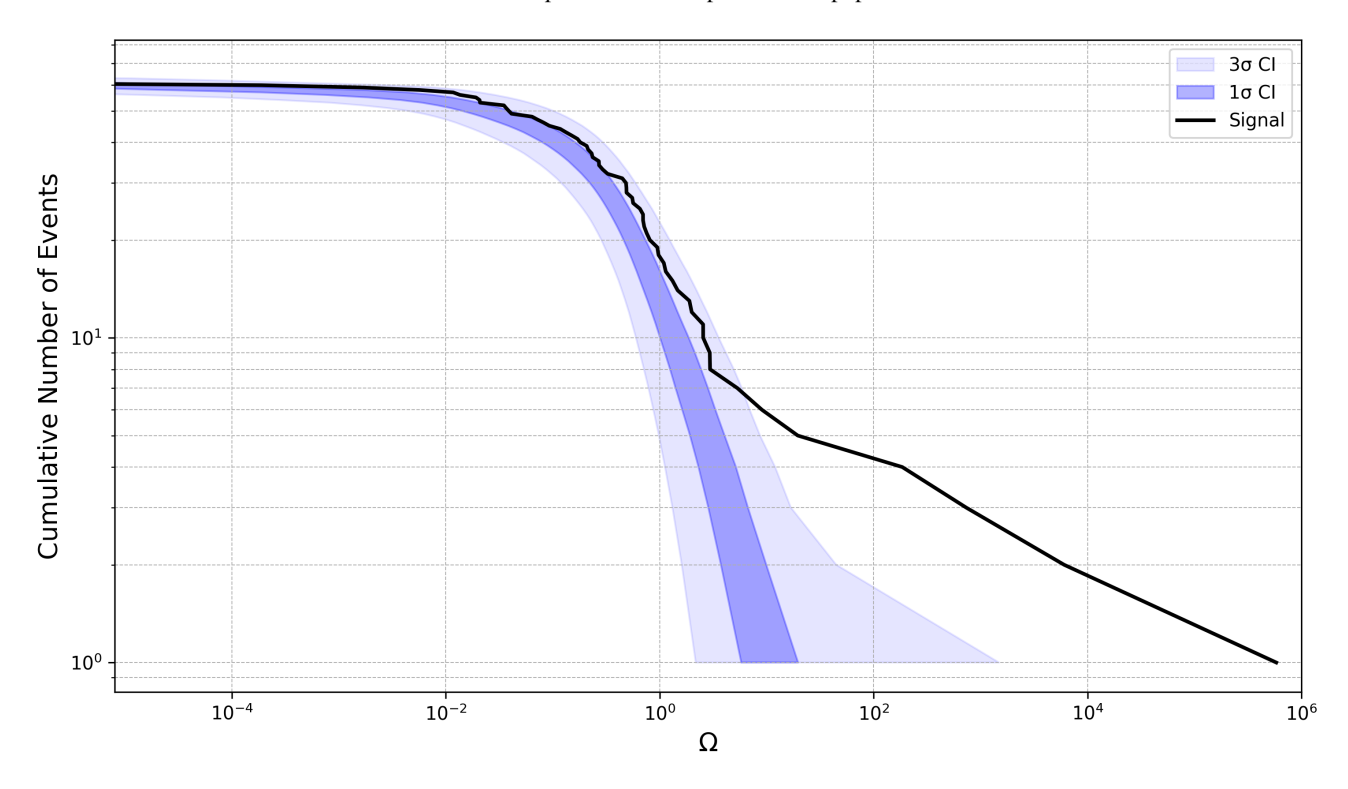


Fig. 2. Cumulative Ω values for the 68 MGF candidates (black line) compared to the background distribution generated from random galaxy rotations. The shaded regions indicate the 1σ (dark blue) and 3σ (light blue) confidence intervals derived from resampling 10,000 background comparisons drawn from an initial set of 45,000 randomized galaxy realizations.

Table 1. Summary of MGF Candidates and Host Galaxy Associations

GRB Name	Ω	Associated	Distance	Association	Fluence	$E_{\rm iso}$
		Galaxy	(Mpc)	(%)	$(\times 10^{-7} \text{ erg cm}^{-2})$	$(\times 10^{44} \text{ erg})$
GRB 231115A	581,513	M82	3.5	>99.9	7.8 ± 0.3	11.5 ± 0.4
GRB 200415A	6041	NGC 253	3.7	>99.9	97 ± 3	142 ± 5
GRB 180128A	734	NGC 253	3.7	>99.9	4.1 ± 0.9	6 ± 1
GRB 120616A	185	IC 0342	2.3	98	3.6 ± 0.3	2.3 ± 0.2
GRB 200423A	20	NGC 6946	7.7	>99.9	12 ± 3	85 ± 20
GRB 231024A	9	NGC 253	3.7	94	3.4 ± 0.4	5.5 ± 0.7
GRB 081213	5	NGC 253	3.7	96	2.6 ± 0.2	4.2 ± 0.3

Notes. GRB 231115A, GRB 200415A, and GRB 180128A are the three known extragalactic MGFs detected by *Fermi/GBM*. Association percentages represent the fraction of the total Ω statistic contributed by the listed host galaxy. Fluence values are in the bolometric range (e.g., 1 keV–10 MeV)

not converting to photon space. As a result, all bursts were implicitly treated as spectrally identical in terms of detectability. It also approximated instrumental sensitivity using a single energy fluence cutoff, and separated the analysis of rate, spectral shape, and detectability into distinct steps, precluding fully self-consistent parameter inference.

To address these limitations, we developed an MCMC implementation that performs posterior inference on key population parameters, the rate of MGFs per solar mass of star formation—or SFR-scaled rate—R, minimum total energetics $E_{\rm iso,min}$, and PL index β for the various samples. For the GBM sample we incorporate a more realistic and physically motivated treatment of spectral variation and detection probability.

3.1. MCMC Modeling: IPN Implementation and Comparison to Burns

This section describes the MCMC model in the context of reproducing the results of Burns et al. (2021) using the same IPN sample and assumptions.

The model begins by assuming that the distribution of $E_{\rm iso}$ for MGFs follows a PL (β) form, where the probability of drawing a given $E_{\rm iso}$ scales as $E_{\rm iso}^{-\beta}$ between a lower cutoff $E_{\rm iso,min}$ and a fixed maximum energy $E_{\rm iso,max}=5.75\times10^{47}$ erg (Burns et al. 2021). The lower cutoff is treated as a free parameter in the model and represents a hard threshold below which there are no events, rather than a soft or exponential turnover. At each MCMC iteration, new values for the β , $E_{\rm iso,min}$, and R (expressed in MGFs per M_{\odot}) are sampled from their respective priors. Using these parameters, a synthetic population of MGFs is generated

Table 2. Summary of Bursts Used in MCMC Modeling

$E_{\rm iso} (10^{44} {\rm erg})$	$E_{\rm p} ({\rm keV})$	α	Sample
~1.2	_	_	NA
4.3	-	_	Burns/IPN
230	850	-0.7	Burns/IPN
530	2150	-0.2	Burns/IPN
16	280	-0.6	Burns/IPN
62	1290	-1.0	Burns/IPN
142	1080	-0.0	Burns/IPN/GBM
6.0	290	-0.6	IPN/GBM
11.5	600	-0.1	IPN/GBM
2.3	500	-0.4	GBM
85	600	-0.7	GBM
5.5	500	-0.8	GBM
4.2	400	-0.6	GBM
	~1.2 4.3 230 530 16 62 142 6.0 11.5 2.3 85 5.5	~1.2	~1.2

Notes. Values for $E_{\rm iso}$ are computed assuming isotropic emission and host galaxy distances. Spectral parameters ($E_{\rm p}$, α) are drawn from time-integrated COMPT model fits where available. The Burns sample refers to all events analyzed in Burns et al. (2021). The IPN sample extends this set by including two additional bursts identified subsequently. The GBM sample comprises all events detected by *Fermi*/GBM, including the four newly reported here.

by first drawing $E_{\rm iso}$ values from the PL distribution. Each burst is then assigned a host galaxy selected with probability proportional to its SFR, using the z=0 Multiwavelength Galaxy Synthesis Catalog (Leroy et al. 2019) limited to a set maximum distance. Finally, the bolometric energy fluence is calculated by assuming isotropic emission and applying inverse-square law scaling, such that $S = E_{\rm iso}/(4\pi D^2)$, where D is the distance to the host galaxy.

Detection is defined as a sharp energy fluence threshold of $2 \times 10^{-6}\,\mathrm{erg\,cm^{-2}}$, consistent with the approach of Burns et al. (2021). Simulated events with bolometric fluence (1 keV–10 MeV) above this threshold are marked as detected, while those below are discarded, and IPN is treated as effectively allsky. The expected number of detections is computed based on the observation time (T_{obs}), completeness, and SFR distribution.

To perform the parameter inference, we use the emcee Python package (Foreman-Mackey et al. 2013), an affine-invariant ensemble sampler that efficiently explores correlated and high-dimensional parameter spaces. We configure the sampler with 80 walkers and 15,000 steps per walker, discarding the first 1,500 steps as burn-in. Walkers are initialized near literature values, with priors drawn from narrow Gaussian distributions centered at $\log_{10}(R*M_{\odot}) \sim -1.3$, $\log_{10}(E_{\rm iso,min}) \sim 43.8\,{\rm erg}$, and $\beta=1.7$. Convergence is assessed using the acceptance fraction, autocorrelation time, and visual inspection of the posterior distributions via corner³ (Foreman-Mackey 2016) plots.

As in Burns et al. (2021), we cannot directly infer a volumetric rate due to the known overdensity of galaxies in the local universe. To account for this and enable comparison with a homogeneous SFR volume, we use the total measured star formation rate within 50 Mpc to convert R into a volumetric rate above a given $E_{\rm iso,min}$.

We apply updated priors (described below) and observation time to the same IPN sample analyzed in Burns et al. (2021). Adopting an observation start date of 21 April 1991, the beginning of concurrent BATSE and *Ulysses* operations, which together enabled extragalactic burst localization, we take $T_{\rm obs}$ =

29,yr. The previously reported values and those obtained with our MCMC method are listed in Table 3.

Priors on the parameters are selected to reflect both physical intuition and empirical constraints, and are implemented as probability distributions within broader hard bounds enforced by the sampler. For the SFR-scaled rate R, we adopt a uniform prior in log-space over the range $\log_{10}(R * M_{\odot}) = [-3, 6]$. The lower limit is motivated by the estimated MGF rate in the Milky Way, while the upper bound exceeds the highest previously inferred extragalactic rates by several ordered of magnitude. For the minimum energy $E_{iso,min}$, we use a uniform prior spanning $10^{42.5}$ erg to $10^{44.1}$ erg. This range includes typical energies of lower-energy recurrent magnetar emissions on the low end, and is truncated at the lowest $E_{\rm iso}$ measured in the observed sample (GRB 790305B; Mazets et al. 1979) on the high end. For the PL index β , we adopt a Gaussian prior centered at 1.7 with a standard deviation of 0.4, with hard bounds at 1.3 and 2.5. This range reflects values explored in Burns et al. (2021) and permits thorough exploration of plausible parameter space without imposing strong biases.

In the five years since the publication of Burns et al. (2021), additional extragalactic MGFs have been identified by the IPN, extending the baseline. We apply the model to this Updated IPN sample, which includes GRB 180128A and GRB 231115A and reflects increased temporal coverage. Incorporating these newer events provides a more complete view of the population and improves statistical power. While this expanded dataset spans multiple instruments and lacks a unified detection efficiency curve, we adopt the same fixed energy fluence threshold methodology as before to ensure consistency with the original analysis. We utilize $T_{\rm obs} = 34\,{\rm yr}$ for this Updated IPN sample. For the SFR distribution, we follow Burns et al. (2021) in including only galaxies within 5 Mpc, as all events identified occurred within that volume.

3.2. Modeling Improvements for GBM Sample

While the IPN-based implementation successfully reproduces prior results, it remains limited by simplifying assumptions re-

³ https://corner.readthedocs.io/en/latest/

garding detection and spectral uniformity. To improve on this, we extend the MCMC framework to model the sample of MGF candidates detected by *Fermi/GBM*. As described in Section 2, GBM's greater sensitivity allows it to detect lower-energy bursts, enabling several key refinements to the population modeling. The GBM events used in this analysis represent previously identified MGFs and the new candidate identifications from this work.

First, we incorporate spectral variation across the population by assigning spectral parameters to each simulated burst. Specifically, the peak energy $E_{\rm p}$ is computed from the burst's isotropic-equivalent energy $E_{\rm iso}$ using a best-fit relation derived from the observed $E_{\rm p}$ – E_{iso} distribution of the full MGF candidate sample (Figure 3), using the fitting method described in Appendix A of (Trigg et al. 2025). The photon index α is assigned as a function of $E_{\rm p}$ using a linear mapping based on observed COMPT fits, wherein higher $E_{\rm p}$ values correspond to $\alpha \sim 0.0$ and lower $E_{\rm p}$ values to $\alpha \sim -1.0$. This theoretically motivated relationship captures the trend seen in known events and is implemented as a piecewise function that increases monotonically with $E_{\rm p}$ and flattens at high energies, ensuring spectral shapes that match observations across the simulated population.

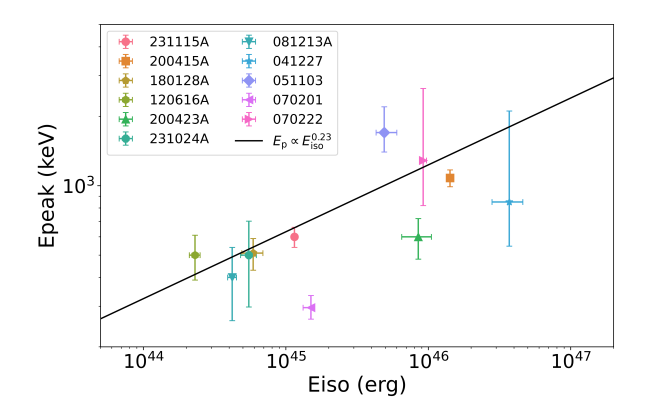


Fig. 3. Peak energy (E_p) versus isotropic energy (E_{iso}) for the sample of extragalactic MGF candidates and confirmed events. Each burst is labeled and color-coded. Error bars reflect uncertainties in both E_{iso} and E_p . The black line shows the best-fit empirical relation. This relation is used to assign E_p values in the population model as a function of E_{iso} .

These spectral parameters are then used to compute photon fluence via a precomputed grid of photon fluence values, derived from COMPT models spanning the relevant $E_{\rm p}$ and α parameter space, as shown in Figure 4. This grid, built from observed MGF spectra, is interpolated using RegularGridInterpolator from the Python package scipy⁴ during MCMC sampling to efficiently convert $E_{\rm iso}$ to photon fluence as a function of both spectral shape and source distance. Photon fluences are then converted to peak photon fluxes assuming a 64 ms integration window, consistent with GBM triggering timescale of GBM.

Detection probabilities are derived from the GBM sensitivity curve (Figure 5) corresponding to its 64 ms trigger window, under the assumption that the full $E_{\rm iso}$ is emitted within this timescale. While GBM employs multiple trigger windows, our efficiency model specifically reflects the 64 ms response. This curve is interpolated to determine characteristic recovery thresholds (e.g., a 50% detection threshold at approximately 3 ph cm⁻² s⁻¹) over the energy range from 50 keV to 300 keV.

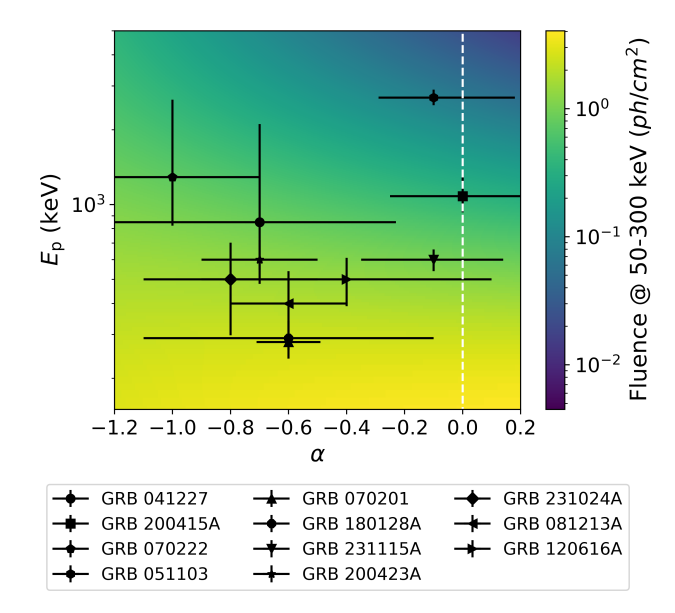


Fig. 4. Normalized fluence scaling surface at $50{\text -}300\,\text{keV}$ as a function of COMPT spectral parameters α and $E_{\rm p}$, constructed using a grid of model spectra and normalized to the observed fluence of GRB 200415A. Overlaid points correspond to observed MGF candidates. Units are relative and do not represent absolute fluence values.

Each event's photon flux is compared with this sensitivity curve to determine the probability of detection, and stochastic realizations are drawn via uniform random sampling. Detection efficiencies are further scaled by GBM's effective sky coverage and observing duty cycle, accounting for a 60% exposure fraction due to limited field of view and periodic passage through the South Atlantic Anomaly, a region where inner radiation belt of Earth dips closest to the surface, resulting in elevated fluxes of energetic particles that expose satellites, including the ISS, to increased ionizing radiation. Additionally, a scaling based on the total observing time of $T_{\rm obs} = 16.72$ years is applied. The farthest event in the GBM sample, GRB 200423A, is located at 7.7 Mpc. Based on this, we conservatively adopt a SFR volume limited to 10 Mpc for the GBM sample. While GBM may in principle be sensitive to extragalactic MGFs out to ~25 Mpc, this more restrictive threshold ensures consistency with the observed sample.

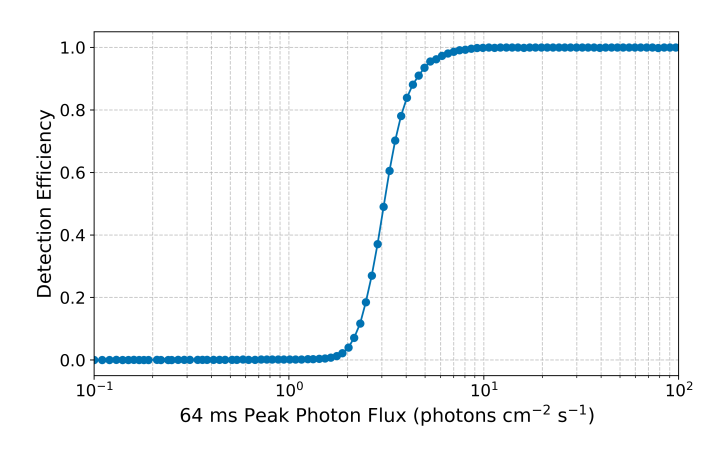


Fig. 5. GBM detection probability as a function of $64 \, \mathrm{ms}$ peak photon flux in the $50\text{--}300 \, \mathrm{keV}$ band.

⁴ https://docs.scipy.org/doc/scipy/reference/generated/scipy.interpolate

3.3. Results from Individual Samples

To quantify the impact of sample selection on the inferred MGF population parameters, we ran independent MCMC analyses on each of the three main data sets: the Burns et al. (2021) IPN sample, the Updated IPN sample (which includes GRB 180128A and GRB 231115A), and the GBM candidate sample identified in this work. Each sample differs in completeness, spectral quality, and instrumental coverage, providing complementary windows into the underlying population.

The Burns et al. (2021) sample consists of six bursts located within 5 Mpc, drawn from IPN detections. As previously stated, to correct for the known galaxy overdensity within this volume, the original results were scaled to the total local SFR within a 50 Mpc sphere. In our analysis, we report volumetric rates scaled to both 50 Mpc and 30 Mpc volumes to enable direct comparison with prior work. However, we adopt 30 Mpc as our preferred normalization distance, as it approximates the scale at which the local universe becomes homogeneous. Additionally, this choice ensures a more complete sampling from the galaxy catalog, as catalog completeness declines with increasing distance. Our modeling uses a galaxy catalog limited to this volume, with simulated events assigned to galaxies in proportion to their total SFR. Best-fit values from the MCMC analysis under each scaling assumption are presented in Tables 3 and 4.

Our MCMC reproduction of the Burns et al. (2021) sample (e.g., MCMC Benchmark) yields posterior distributions that closely match the original study, validating the consistency of our approach. Across all three instrument-specific samples, the inferred values of β are mutually consistent within uncertainties, lending additional confidence to the robustness of the population-level constraints. The inferred $E_{iso,min}$ differs across samples due to differences in sensitivity and modeling assumptions, and the corresponding volumetric rates reflect the number of MGFs expected above the respective thresholds. Notably, the shift from a 50 Mpc to 30 Mpc scaling distance leads to systematically higher inferred rates. This is an expected outcome, given that the SFR measurement are imcomplete and get worse with distance. The total SFR enclosed within 30 Mpc is smaller (~ $1400 M_{\odot} yr^{-1}$ at 30 Mpc compared to ~ $4000 M_{\odot} yr^{-1}$ at 50 Mpc), requiring a higher intrinsic rate per unit volume to reproduce the observed number of events.

The Updated IPN sample incorporates more recently confirmed MGFs and spans a longer observational baseline, resulting in improved completeness. The addition of GRB 180128A and GRB 231115A, along with updated model parameters, yields an inferred β that remains consistent with previously published values and with results from the other MCMC fits. The inferred $E_{\rm iso,min}$ is a factor of four lower than in the Burns (2021) MCMC benchmark, while the corresponding SFR-scaled rate R increases.

The GBM candidate sample includes the majority of bursts in the modeled dataset and benefits from uniform detection conditions and a well-characterized sensitivity curve. The inferred β remains consistent with those derived from the IPN analyses, while the lower value of $E_{\rm iso,min}$ reflects enhanced sensitivity of GBM to lower-energy events.

3.4. Results from the Joint Sample

In addition to the individual sample fits, the Joint MCMC model yields a set of posterior distributions that incorporate all observed bursts within a unified framework. Simulated events are passed through the same population-level energy distribution as

before, but evaluated under both GBM and IPN detection criteria. For each instrument, the predicted number of detections is computed independently based on the appropriate exposure, sensitivity, and completeness scaling. To account for overlapping detections, the expected number of joint detections is calculated using the intersection of the instrument-specific limiting factors: the IPN-limited galaxy subset and completeness, and the GBM-limited detection efficiency and observing time. This overlap in detections is subtracted from the combined total to avoid double-counting.

The Joint posterior places tighter bounds on the SFR-scaled rate R and exhibits a preferred value of β that is consistent with Burns et al. (2021) and theoretical expectations. These constraints, summarized in Table 3 and Table 4, represent the most statistically robust inference in this study. The full posterior distributions are shown in Figure 6, and we adopt the Joint fit as our preferred model for subsequent discussion.

For the convenience of the reader, we also report two additional Joint-fit results under physically motivated parameter constraints. First, fixing $E_{\rm iso,min}=1.2\times10^{44}\,\rm erg$ –corresponding to the lowest E_{iso} observed among known MGF candidates–yields a volumetric rate of $5.5^{+4.5}_{-2.7}\times10^5\,\rm Gpc^{-3}$ yr⁻¹ with $\beta=1.76^{+0.25}_{-0.26}$. Second, fixing both $E_{\rm iso,min}$ to this value and $\beta=1.7$, which is broadly consistent with all other fits, yields a rate estimate of $5.05^{+2.88}_{-2.09}\times10^5\,\rm Gpc^{-3}$ yr⁻¹. This latter result reflects the most conservative estimate of the extragalactic MGF rate, based on physically motivated assumptions consistent with the broader set of fits.

The similarity of inferred population parameters across the IPN, GBM, and Joint samples supports the plausibility that the candidate events originate from the same physical process. While not definitive, this consistency strengthens the case that these bursts are compatible with an MGF interpretation, given their alignment with both theoretical expectations and properties of known MGFs. Importantly, the agreement between the GBM sample, in which selection was based purely on temporal and spectral criteria, and the IPN sample with independent localizations provides strong validation for our GBM-based event selection method and the population modeling framework developed in this work.

4. Discussion

With an observational sample and a physically motivated forward-folding modeling framework, we use the Joint MCMC model to infer key properties of the extragalactic MGF population. These results constrain the intrinsic distribution of isotropic-equivalent burst energetics, the volumetric rate of detectable events, and their connection to magnetar formation channels and recurrence behavior. Together, they offer insight into how the inferred population properties relate to progenitor demographics, observed Galactic activity, and the broader diversity of magnetar-driven high-energy transients.

4.1. Intrinsic Energetics Distribution

Our MCMC analysis adopts the same PL functional form for the distribution of $E_{\rm iso}$ used in Burns et al. (2021), parameterized by a slope β , a maximum energy cutoff $E_{\rm iso,max}$, and a minimum energy cutoff $E_{\rm iso,min}$. Across all three samples–Burns IPN, Updated IPN, and GBM–the inferred PL slopes are in good agreement with the $\beta \sim 1.7$ index reported by Burns et al. (2021) (see Table 3). This consistency holds despite differences in sample size, detection thresholds, and completeness modeling. The

Table 3. Posterior Parameter Estimates from MCMC Fits to Individual Samples

Sample	R	β	$E_{ m iso,min}$
	(M_{\odot}^{-1})		$(\times 10^{43} \text{ erg})$
Burns (2021) Results	$0.05^{+0.05}_{-0.04}$	$1.7^{+0.4}_{-0.4}$	37
Burns (2021) MCMC Benchmark	$0.05^{+0.14}_{-0.04}$	$1.78^{+0.43}_{-0.37}$	16^{+24}_{-15}
Burns (2021) IPN MCMC	$0.07^{+0.16}_{-0.05}$	$1.64^{+0.34}_{-0.30}$	$4.2^{+6.8}_{-3.5}$
Updated IPN MCMC	$0.09^{+0.16}_{-0.06}$	$1.67^{+0.31}_{-0.29}$	$5.0^{+6.2}_{-4.1}$
GBM MCMC	$0.06^{+0.08}_{-0.03}$	$1.72^{+0.21}_{-0.19}$	$3.7^{+5.0}_{-2.6}$
Joint MCMC	$0.07^{+0.10}_{-0.04}$	$1.67^{+0.26}_{-0.25}$	$5.6^{+5.7}_{-4.7}$

Notes. Posterior estimates for the SFR-scaled rate R, PL index β , and minimum isotropic-equivalent energy $E_{\rm iso,min}$ from MCMC fits to individual and joint MGF samples. "Burns (2021) Results" are the values from the Burns et al. (2021) analysis. "Burns (2021) MCMC Benchmark" are the results from the MCMC fitting using the Burns et al. (2021) sample and posteriors. "Burns (2021) IPN MCMC" uses the Burns et al. (2021) samples with our posterior assumptions and the updated $T_{\rm obs}$. "IPN MCMC" incorporates additional IPN and GBM candidates GRB 180128A and GRB 231115A. Values are reported at the 90% confidence level.

Table 4. Scaled Volumetric Rates

Sample	Scaling Distance	Volumetric Rate
	(Mpc)	$(\times 10^5 \mathrm{Gpc^{-3} yr^{-1}})$
Burns (2021) Results	50	$3.8^{+4.0}_{-3.1}$
Burns (2021) MCMC Benchmark	50	$3.9^{+4.4}_{-2.0}$
Burns (2021) IPN MCMC	50	$5.6^{+\overline{5.9}}_{-2.9}$
Updated IPN MCMC	50	$6.6^{+6.0}_{-3.2}$
Burns (2021) IPN MCMC	30	$8.7^{+9.9}_{-4.9}$
IPN MCMC	30	$11.2^{+9.9}_{-4.9}$
GBM MCMC	30	$8.0^{+9.4}_{-4.0}$
Joint MCMC	30	$8.2^{+6.2}_{-3.2}$

Notes. Volumetric rate estimates derived from MCMC fits to individual and joint samples, scaled to the star formation rate within the indicated distance. The original Burns et al. (2021) sample is shown separately, while the Updated IPN and GBM samples, along with the combined joint model, highlighted in yellow, represent the results of the analysis presented in this work.

robustness of this result across distinct instruments and modeling assumptions reinforces the conclusion that MGFs follow a moderately steep energetics distribution, in line with both theoretical expectations and prior observations of lower-energy magnetar flares. In particular, the inferred PL slope of $\beta \sim 1.7$ is remarkably consistent with the predictions of starquake-driven models of magnetar activity, in which crustal strain builds up and is episodically released in discrete energy bursts, analogous to earthquakes (Cheng et al. 1996). This distribution matches the Gutenberg-Richter PL (β =1.66) seen in terrestrial seismic activity, and is reproduced in magnetar burst observations such as those from SGR 1806-20, where fluence distributions measured over years of INTEGRAL data exhibit a similar slope (Götz et al. 2006). The close alignment of the observed MGF E_{iso} distribution with these theoretical models provides compelling support for the view that magnetic stress-induced starquakes in the NS crust drive MGFs.

The inferred values of $E_{\rm iso,min}$ vary across samples. The GBM-only model yields the lowest threshold, $E_{\rm iso,min} \sim 3.7^{+5.0}_{-2.7} \times 10^{43}$ erg, while the Updated IPN model returns a slightly higher value of $E_{\rm iso,min} \sim 5.0^{+6.2}_{-4.1} \times 10^{43}$ erg. The Joint fit converges at a value of $5.6^{+5.7}_{-4.7} \times 10^{43}$ erg. While these differences may loosely correspond to the sensitivity and sampled detection volume of each instrument, the $E_{\rm iso,min}$ posteriors are primarily shaped by the absence of lower- $E_{\rm iso}$ events within the effective volume of each survey. In all cases, the constraints favor relatively high

threshold values, near the upper end of the prior range (see Figure 6), indicating that the current data sets lack sufficient spacetime volume to tightly constrain the low end of the MGF $E_{\rm iso}$ distribution.

4.2. Temporal Structure in MGF Peak Emissions

A reasonable fraction of the identified candidates exhibit temporally complex emission. Approximately 40% of the extragalactic sample display multiple statistically distinct pulses. This confirms that MGFs can show multi-pulsed temporal structure, a property previously documented primarily in lower-energy magnetar bursts. These findings extend the known diversity of MGF temporal behavior and demonstrate that the presence of multiple pulses is not inconsistent with a magnetar origin. While burst morphology remains a valuable discriminant in candidate selection-particularly features such as millisecond variability and hard initial spikes-it cannot, on its own, conclusively confirm or exclude an MGF origin. Instead, temporal structure must be considered alongside spectral properties, energetics, and spatial coincidence with star-forming galaxies within a comprehensive, multi-dimensional classification framework, as adopted throughout this analysis.

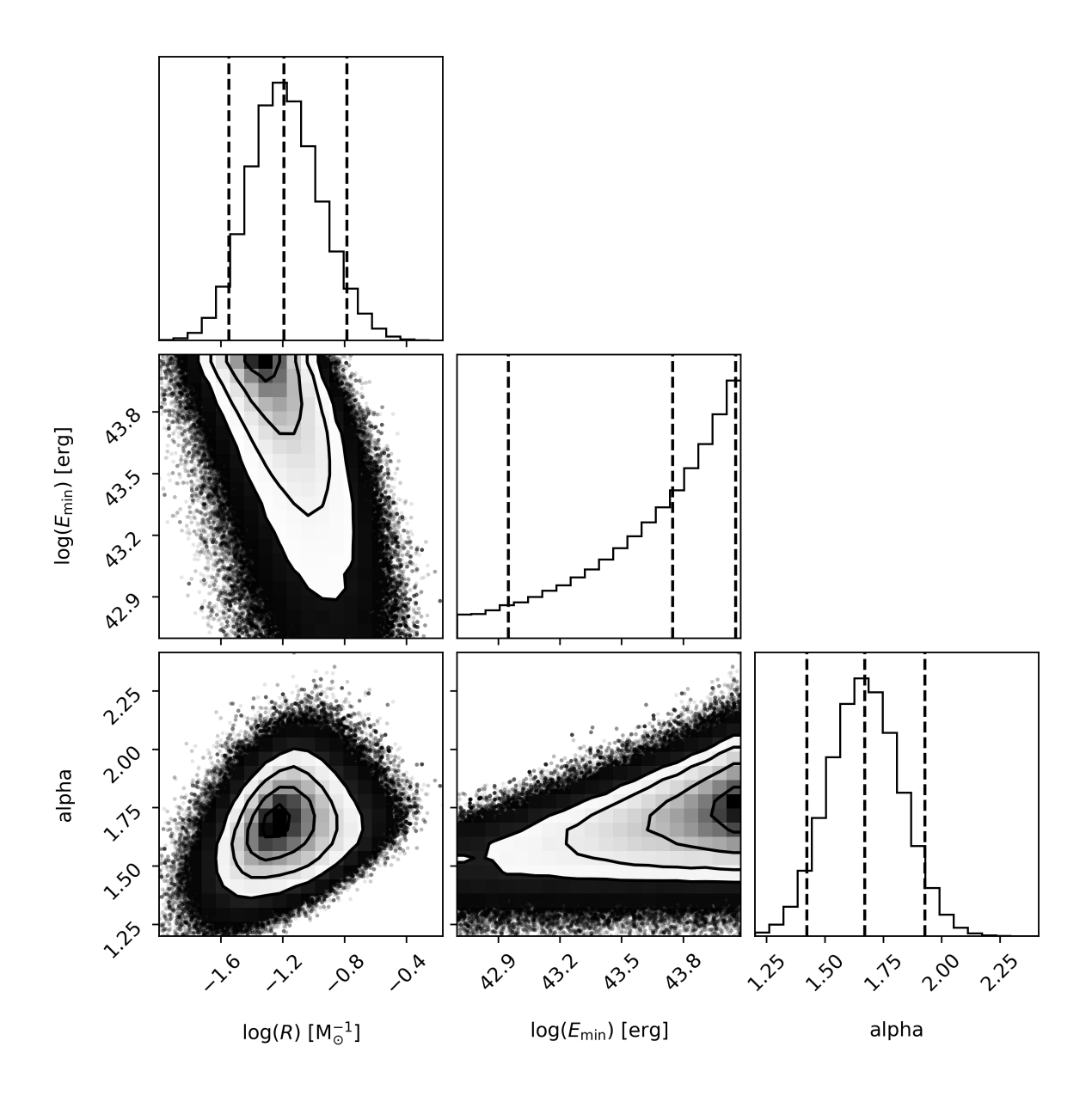


Fig. 6. Posterior distributions from the Joint MCMC fit to the combined IPN and GBM samples, showing the marginalized one- and two-dimensional distributions for the model parameters: the SFR-scaled rate $\log_{10} R$, $\log_{10} E_{\rm iso,min}$, and α . Contours in the 2D plots represent 1σ , 2σ , and 3σ credible regions. These results represent the best-constrained model from the full joint population analysis, incorporating both spectral and detection completeness effects across instruments.

4.3. Volumetric Rate and Event Recurrence

The Joint MCMC model represents our preferred estimate of the extragalactic MGF population, incorporating both GBM and IPN detections into a unified likelihood framework. It yields a volumetric rate of $8.2^{+6.2}_{-3.2} \times 10^5$ Gpc⁻³ yr⁻¹, scaled to the total SFR within 30 Mpc. The rate should be understood in the context of the fitted energetics threshold ($E_{\rm iso,min}$) of the model, as determined by the posterior distribution. The reported rate is not an absolute, independent quantity, but rather reflects the occurrence of MGFs with $E_{\rm iso}$ values above the inferred $E_{\rm iso,min}$ within the modeled population. Because $E_{\rm iso,min}$ is itself a fitted parameter, the inferred rate is conditional on that threshold, making direct comparisons between models with different values nontrivial.

When scaled by the combined star formation rate of the Milky Way and LMC ($\sim 1.95~\rm M_{\odot}~\rm yr^{-1}$), the inferred SFR-scaled rate R implies a Galactic occurrence rate of approximately $0.14^{+0.20}_{-0.08}~\rm yr^{-1}$. Under the assumption of a stationary Poisson process, this corresponds to an expectation of Galactic events over the last 57 years of $0.14^{+0.20}_{-0.08}~\rm yr^{-1}\times 57~\rm yr=8^{+11}_{-5}$. In contrast, only 3 such events have been observed in that interval. The probability of observing 3 or fewer events given this expectation is approximately 4.3%, indicating mild ($\sim 2\sigma$) tension. Our fitted $E_{\rm iso,min}$ values may reflect an incomplete sampling of the intrinsic burst energetics, particularly at the low end of the energetics distribution. Future observations are needed to determine whether the apparent overprediction results from selection effects, misclassified bursts, or a break in the underlying distribution.

Following Tendulkar et al. (2016), we compare the inferred volumetric MGF rate to the expected rate of progenitor formation, which can be expressed as

$$R_{\text{MGF}} = R_{\text{Event}} f_{\text{M}} \tau_{\text{Active}} r_{\text{MGF/M}} \tag{1}$$

Here, $R_{\rm Event}$ is the rate of progenitor events capable of forming magnetars, $f_{\rm M}$ is the fraction of those events that successfully produce magnetars, $\tau_{\rm Active}$ is the timescale over which magnetars can produce giant flares, and $r_{\rm MGF/M}$ is the rate of MGFs per magnetar per unit time. We adopt $\tau_{\rm Active} \approx 10^4$ yr, consistent with the decay timescale of the magnetic field as estimated by Beniamini et al. (2019).

If we assume that CCSN is the only progenitor channel, and that all CCSN produce magnetars, then $R_{\rm events} = R_{\rm CCSN} = 7 \times 10^4 \, {\rm Gpc^{-3} \, yr^{-1}}$ (Li et al. 2011) and $f_{\rm M} = 1$. Using the lower bound found for our Joint volumetric rate $(4.9 \times 10^5 \, {\rm Gpc^{-3} \, yr^{-1}})$, the average magnetar (at 90% confidence) must produce at least $r_{\rm MGF/M} = 7$ giant flares over an average active lifetime. This represents the first empirical lower bound on the number of MGFs expected per magnetar, providing a new constraint on their recurrence behavior that is directly informed by volumetric event rates.

4.4. Assessing MGFs as a Source of Fast Radio Bursts

Only one Galactic magnetar, SGR 1935+2154, has been observed to emit an FRB-like radio burst contemporaneously with a soft X-ray event (FRB 200428), though the energy of the flare was well below the MGF regime (Bochenek et al. 2020; Mereghetti et al. 2020). Beniamini et al. (2025) emphasize that while such events may arise during magnetar short bursts, there is no evidence that classical MGFs routinely generate FRBs, and many of the brightest MGFs lack any associated radio signature. Supporting this, Principe et al. (2023) found no gammaray counterparts to known FRBs in a dedicated search using Fermi/LAT. However, one oddity in this Galactic FRB–SGR association is that the FRB itself was sub-energetic compared to the broader cosmological FRB sample. If the FRB and SGR emission energetics scale together, this suggests that more distant FRBs may arise from more energetic flares motivating the consideration of MGFs as potential FRB progenitors. This, together with the mismatch in volumetric rates, indicates that if magnetars do produce FRBs, only a rare subset are responsible.

The volumetric rate inferred from the Joint MCMC model is notably higher than most published estimates of the FRB event rate. For instance, James et al. (2022) report a volumetric rate of FRBs above 10^{39} erg of $\Phi_{39}=8.7^{+1.7}_{-3.9}\times10^4$ Gpc $^{-3}$ yr $^{-1}$, based on CHIME detections. When compared to the MGF rate derived in this work, this suggests that at most $\sim 10^{-2}$ of MGFs could be accompanied by detectable FRB emission, assuming any are associated at all. Importantly, this should be interpreted as an upper limit on the fraction of MGFs that could produce FRBs; the true value could be substantially lower, or zero, depending on the physical mechanism and emission geometry involved.

5. Conclusion

Our refined search of archival *Fermi*/GBM data, guided by observationally informed selection criteria, yielded four additional MGF candidates, thereby expanding the extragalactic sample and enhancing the statistical power available for population modeling.

The clear positive correlation observed between total isotropic energy ($E_{\rm iso}$) and spectral peak energy ($E_{\rm p}$), incorporated into the MCMC framework, enables realistic variation in spectral shape across the population and addresses a significant limitation of prior analyses, which assumed fixed spectral parameters. All three instrument-specific MCMC fits—the Burns IPN, Updated IPN, and GBM-only samples—yield consistent posterior distributions for R and β within uncertainties. Minor differences in inferred parameters are attributed to statistical variation between samples, as the modeling framework explicitly accounts for each instrument's sensitivity and selection effects. This consistency across independent datasets reinforces the robustness of the inferred MGF population parameters.

The Joint MCMC model represents the most comprehensive and self-consistent inference of the extragalactic MGF population to date. By combining the GBM and IPN samples under a unified likelihood function, the model accounts for distinct detection criteria, selection effects, and completeness functions for each instrument. The resulting joint posterior places tighter constraints on the volumetric rate, likely reflecting the broader spacetime volume and increased sample size accessible in the combined analysis.

The inferred volumetric rate implies that MGFs are relatively common in star-forming galaxies, consistent with a CCSN origin. The rate requires that each source emit multiple flares above over its active lifetime, reinforcing recurrence as a fundamental aspect of magnetar evolution. This recurrence requirement places strong constraints on alternative progenitor channels which occur too infrequently to account for the observed population without invoking implausibly high flare rates per source.

The high MGF rate also exceeds current estimates of the FRB volumetric event rate, suggesting that only a small fraction, on the order of 10⁻², of MGFs produce observable FRBs. These findings imply that while MGFs may serve as progenitors for some FRBs, the radio-bright subset represents only a small fraction of the broader magnetar flare population.

Several of the newly identified GBM candidates are sufficiently bright to warrant searches for potential additional detections to improve IPN localizations, which could help mitigate the relatively poor localization precision of GBM. Adapting our search algorithm to instruments like BATSE may yield further candidates, while extending the approach to current instruments like GBM and future observatories such as the Compton Spectrometer and Imager (COSI; Tomsick et al. 2024) could enable real-time classification and facilitate X-ray follow-up aimed at detecting the elusive modulated tail, the smoking-gun signature of MGFs. The results presented here demonstrate the power of unified, instrument-sensitive modeling frameworks for understanding rare astrophysical populations. With the validation of the Joint inference model and the incorporation of spectral and flux-dependent detectability, future work can now focus on refining the inferred luminosity function, constraining recurrence statistics, and clarifying the role of MGFs in high-energy transient astrophysics.

Acknowledgements. The USRA co-authors gratefully acknowledge NASA funding from cooperative agreement 80NSSC24M0035. E.N. acknowledges NASA funding through Cooperative Agreement 80NSSC22K0982. O.J.R. graciously acknowledges NASA funding support from Fermi GI large grant 80NSSC21K2038.

References

Abbott, B., Abbott, R., Adhikari, R., et al. 2007, Physical Review D, 76, 062003

- Abbott, B. P., Abbott, R., Abbott, T. D., et al. 2017a, Physical Review Letters, 118, 221101
- Abbott, B. P., Abbott, R., Abbott, T. D., et al. 2017b, Physical Review Letters, 119, 141101
- Abbott, B. P. et al. 2019, The Astrophysical Journal, 874, 163
- Aptekar, R. L., Frederiks, D. D., Golenetskii, S. V., et al. 1995, Space Science Reviews, 71, 265
- Barthelmy, S. D., Barbier, L. M., Cummings, J. R., et al. 2005, Space Science Reviews, 120, 143
- Beniamini, P., Hotokezaka, K., van der Horst, A., & Kouveliotou, C. 2019, Monthly Notices of the Royal Astronomical Society, 487, 1426
- Beniamini, P., Wadiasingh, Z., Trigg, A., et al. 2025, The Astrophysical Journal, 980, 211
- Bochenek, C. D., Ravi, V., Belov, K. V., et al. 2020, Nature, 587, 59
- Burbidge, E. M., Burbidge, G. R., Fowler, W. A., & Hoyle, F. 1957, Rev. Mod. Phys., 29, 547
- Burns, E., Svinkin, D., Hurley, K., et al. 2021, ApJ, 907, L28
- Burns, E., Veres, P., Connaughton, V., et al. 2018, ApJ, 863, L34
- Cameron, A. G. 1957, Stellar evolution, nuclear astrophysics, and nucleogenesis. Second edition, Tech. rep., Atomic Energy of Canada Ltd., Chalk River, Ontario (Canada)
- Cehula, J., Thompson, T. A., & Metzger, B. D. 2024, Monthly Notices of the Royal Astronomical Society, 528, 5323
- Cheng, B., Epstein, R. I., Guyer, R. A., & Young, A. C. 1996, Nature, 382, 518 Curtin, A. P. & Chime/FRB Collaboration. 2023, GRB Coordinates Network,
- Duncan, R. C. 2001, in American Institute of Physics Conference Series, Vol. 586, 20th Texas Symposium on relativistic astrophysics, ed. J. C. Wheeler & H. Martel (AIP), 495–500
- Duncan, R. C. & Thompson, C. 1992, The Astrophysical Journal, 392, L9 Eichler, D., Livio, M., Piran, T., & Schramm, D. N. 1989, Nature, 340, 126
- Feroci, M., Frontera, F., Costa, E., et al. 1999, ApJ, 515, L9
- Fong, W., Berger, E., Margutti, R., & Zauderer, B. A. 2015, The Astrophysical Journal, 815, 102
- Foreman-Mackey, D. 2016, The Journal of Open Source Software, 1, 24
- Foreman-Mackey, D., Hogg, D. W., Lang, D., & Goodman, J. 2013, Publications of the Astronomical Society of the Pacific, 125, 306
- Frederiks, D. D., Golenetskii, S. V., Palshin, V. D., et al. 2007a, Astronomy Letters, 33, 1
- Frederiks, D. D., Palshin, V. D., Aptekar, R. L., et al. 2007b, Astronomy Letters, 33, 19
- Gaensler, B. M. 2004, Advances in Space Research, 33, 645
- Goldstein, A. et al. 2017, The Astrophysical Journal Letters, 848
- Götz, D., Mereghetti, S., Molkov, S., et al. 2006, Astronomy & Astrophysics, 445, 313
- Gruber, D., Goldstein, A., von Ahlefeld, V. W., et al. 2014, The Astrophysical Journal Supplement Series, 211, 12
- Hurley, K. 2011, Advances in Space Research, 47, 1337
- Hurley, K., Boggs, S. E., Smith, D. M., et al. 2005, Nature, 434, 1098
- Hurley, K., Cline, T., Mazets, E., et al. 1999, Nature, 397, 41
- Hurley, K., Mitrofanov, I. G., Golovin, D., et al. 2013, in EAS Publications Series, Vol. 61, EAS Publications Series, ed. A. J. Castro-Tirado, J. Gorosabel, & I. H. Park (EDP), 459-464
- Hurley, K., Rowlinson, A., Bellm, E., et al. 2010, Monthly Notices of the Royal Astronomical Society, 403, 342
- James, C. W., Prochaska, J. X., Macquart, J. P., et al. 2022, Monthly Notices of the Royal Astronomical Society, 510, L18
- Kaspi, V. M. & Beloborodov, A. M. 2017, Annual Review of Astronomy & Astrophysics, 55, 261
- Kouveliotou, C., Meegan, C. A., Fishman, G. J., et al. 1993, The Astrophysical Journal Letters, 413, L101
- Kouveliotou, C., Wijers, R. A., & Woosley, S. 2012, Gamma-ray Bursts, Vol. 51 (Cambridge University Press)
- Leroy, A. K., Sandstrom, K. M., Lang, D., et al. 2019, The Astrophysical Journal Supplement Series, 244, 24
- Li, W., Chornock, R., Leaman, J., et al. 2011, Monthly Notices of the Royal Astronomical Society, 412, 1473
- Macquet, A., Bizouard, M.-A., Burns, E., et al. 2021, The Astrophysical Journal, 918, 80
- Mazets, E., Golenetskii, S., Il'Inskii, V., Aptekar', R., & Guryan, Y. A. 1979, Nature, 282, 587
- Mazets, E. P., Aptekar, R. L., Cline, T. L., et al. 2008, The Astrophysical Journal, 680, 545
- Mazets, E. P., Golenetskii, S. V., Gurian, I. A., & Ilinskii, V. N. 1982, Ap&SS, 84, 173
- Mazets, E. P., Golentskii, S. V., Ilinskii, V. N., Aptekar, R. L., & Guryan, I. A. 1979, Nature, 282, 587
- Meegan, C., Lichti, G., Bhat, P., et al. 2009, The Astrophysical Journal, 702, 791 Mereghetti, S., Rigoselli, M., Salvaterra, R., et al. 2024, Nature, 629, 58

- Mereghetti, S., Savchenko, V., Ferrigno, C., et al. 2020, The Astrophysical Journal Letters, 898, L29
- Negro, M. & Burns, E. 2023, in Neutron Star Astrophysics at the Crossroads: Magnetars and the Multimessenger Revolution, ed. E. Troja & M. G. Baring, Vol. 363, 284-287
- Negro, M., Younes, G., Wadiasingh, Z., et al. 2024, Frontiers in Astronomy and Space Sciences, Volume 11 - 2024
- Ofek, E. O., Kulkarni, S., Nakar, E., et al. 2006, The Astrophysical Journal, 652, 507
- Ofek, E. O., Muno, M., Quimby, R., et al. 2008, The Astrophysical Journal, 681, 1464
- Olausen, S. A. & Kaspi, V. M. 2014, The Astrophysical Journal Supplement Series, 212, 6
- Paczynski, B. 1992, Acta Astron., 42, 145
- Palmer, D. M., Barthelmy, S., Gehrels, N., et al. 2005, Nature, 434, 1107
- Patel, A., Metzger, B. D., Cehula, J., et al. 2025, Direct evidence for r-process nucleosynthesis in delayed MeV emission from the SGR 1806-20 magnetar
- Patra, N. K., Malik, T., Sen, D., Jha, T. K., & Mishra, H. 2020, The Astrophysical Journal, 900, 49
- Popov, S. B., Postnov, K. A., & Pshirkov, M. S. 2018, Physics-Uspekhi, 61, 965 Principe, G., Di Venere, L., Negro, M., et al. 2023, Astronomy & Astrophysics, 675, A99
- Punturo, M., Abernathy, M., Acernese, F., et al. 2010, Classical and Quantum Gravity, 27, 194002
- Roberts, O. J., Veres, P., Baring, M. G., et al. 2021, Nature, 589, 207
- Scargle, J. D., Norris, J. P., Jackson, B., & Chiang, J. 2013, ApJ, 764, 167
- Stevenson, D. J. 2008, Nature, 451, 261
- Svinkin, D., Frederiks, D., Hurley, K., et al. 2021, Nature, 589, 211
- Svinkin, D. S., Frederiks, D. D., Aptekar, R. L., et al. 2016, The Astrophysical Journal Supplement Series, 224, 10
- Tendulkar, S. P., Kaspi, V. M., & Patel, C. 2016, The Astrophysical Journal, 827,
- Thompson, C. & Duncan, R. C. 1995, Monthly Notices of the Royal Astronomical Society, 275, 255
- Thompson, C. & Duncan, R. C. 1996, The Astrophysical Journal, 473, 322
- Tomsick, J., Boggs, S., Zoglauer, A., et al. 2024, in 38th International Cosmic Ray Conference, 745
- Trigg, A. C., Burns, E., Roberts, O. J., et al. 2024, A&A, 687, A173
- Trigg, A. C., Stewart, R., Van Kooten, A., et al. 2025, A&A, 694, A323
- Usov, V. V. 1984, Astrophysics and Space Science, 107, 191